

Compact Air Bearing Spindles for Desktop Sized Machine Tools

Christopher Müller, Benjamin Kirsch and Jan C. Aurich

Abstract In this paper two new small and lightweight spindles for the implementation in desktop sized machine tools are introduced. In both spindles, the tool shaft with a micro tool on the tip (e.g. micro end mill, micro pencil grinding tool or Electrical Discharge Machining (EDM) electrode) works directly as a rotor and is supported by aerostatic bearings. The spindles are driven via air turbines and reaches high rotational speeds in combination with high rotational accuracies. One spindle was implemented in a desktop-sized machine tool and used for micro machining of titanium and brass. With the high rotational speed of the spindles very high material removal rates can be achieved. Thus, the productivity of the micro machining process is enhanced.

1 Introduction

Increasing demands on the miniaturisation of components and functionalisation of component surfaces require high manufacturing accuracy and economic processes [1]. An efficient way to produce parts in the micro range and micro-structured surfaces is micro machining, with micro end mills [2] and micro pencil grinding tools [3] on Ultra Precision (UP) machine tools. The commercially available UP machine tools used for micro machining exceed the size of components and micro structures by several orders of magnitude [4]. Commonly, the workpieces are very small, with sizes under $100 \times 100 \text{ mm}^2$ and the micro tool's, e.g. micro end mills or micro pencil grinding tools [5], diameter range is between $3 \mu\text{m}$ and 3 mm . To minimise the installation space and improve the dynamic properties of the axis, much smaller

C. Müller (✉) · B. Kirsch · J.C. Aurich
Institute for Manufacturing Technology and Production Systems (FBK),
University of Kaiserslautern, Kaiserslautern, Germany
e-mail: fbk@mv.uni-kl.de

© Springer International Publishing AG 2017
J.P. Wulfsberg and A. Sanders (eds.), *Small Machine Tools
for Small Workpieces*, Lecture Notes in Production Engineering,
DOI 10.1007/978-3-319-49269-8_2

workpiece-size and micro tool-size adapted machine tools are required. To achieve this minimisation and improvement of the performance of machine tools, new small and lightweight parts have to be developed [6].

The major component of a machine tool is the main spindle. To reach the required cutting speed in micro milling, the rotational speed of the spindles needs to be increased significantly, compared to spindles, which are used for conventional machining [7]. Spindles designed for micro machining are usually electric motor-driven or air turbine-driven. Air turbine-driven spindles have the advantage of less installation space and require no power electronics, compared to the electrically driven one. The control of the rotational speed and torque is basically a function of the mass flow rate adjusted by a valve. Additionally, the air turbine components are relatively inexpensive to manufacture [8].

Several studies have been performed on spindles for micro machining. Gill et al. developed a spindle, which uses a commercially available spindle combined with a friction drive system [9]. The spindle achieves a maximum speed of 500,000 rpm and a radial tool run-out of 25 μm , which is not feasible for micro machining. The spindle designed by Sung et al. is driven by an air turbine and has a maximum speed of 422,400 rpm [10]. A shape memory alloy-based clamping system with a radial run-out of 3.2 μm was used. Delhaes et al. applied a novel viscous drive mechanism in their spindle and reach a rotational speed of only 24,000 rpm [11]. The rotor in the spindle has no turbine blades, the drive torque is only generated by a tangential flow generated by nozzles. Jahanmir et al. developed an air bearing spindle, which reaches a rotational speed of approx. 500,000 rpm [12]. The rotor in the spindle is supported by aerodynamic foil bearings and the tool is shrink fitted onto the rotor, which results in a low run-out error of 2.5 μm . Machining tests with this spindle revealed disadvantages concerning the stiffness of the foil air bearings. Which is not stiff enough for the feed normal force initiated by the micro end mill [13]. Kimman et al. use active magnetic bearings in their motor-driven spindle [14]. The spindle reaches 125,000 rpm with a tool run-out of 7.5 μm . Li et al. developed a novel mechanism to improve the radial tool run-out of spindles [15]. A monolithic flexible coupling was used to decouple the turbine shaft and the tool. In this case, the tool shank is directly supported by aerostatic bearings, which can minimise the run-out of the tool at high speeds. This spindle reaches 240,000 rpm with a tool run-out of 2.79 μm . Table 1 presents an overview of the spindles developed for micro machining applications.

Commercially available spindles are offered e.g. from ABL, Westwind and Aerolas. These spindles are results of the Printed Circuit Boards (PCB) industry and are used for drilling micro holes into the boards. They reach maximum rotational speeds of up to 300,000 rpm with tool run-outs in the lower two-digit micro meter range.

Although nearly all spindles presented reach sufficient rotational speeds for micro machining, their rotational accuracy is not satisfactory. The radial run-out of a few commercially available spindles has advanced to the micron level, but their speed is generally less than 200,000 rpm [15]. In addition, the size of most spindles is relatively large, unsuitable for the implementation in desktop-sized machine tools.

In this study, high-speed and precision spindles for micro machining applications are presented. The rotors in the spindles are driven by air turbines and supported

Table 1 Overview of developed spindles for micro machining (DN number = rotational speed/rpm · rotor diameter/mm)

Author	Max. rotational speed/rpm	Rotor dia./mm	DN number	Tool run-out/ μm	Bearing type	Drive system
Gill et al. (2004)	500,000	3.175	1,587,500	25	Aerostatic	Motor
Sung (2007)	422,000	7	2,954,000	3.2	Aerostatic	Air turbine
Delhaes et al. (2009)	24,000	6	144,000	n.a.	Aerostatic	Viscous
Jahanmir et al. (2010)	450,000	6	2,700,000	2.5	Aerodynamic	Air turbine
Kimm (2010)	125,000	12	1,500,000	7.5	Magnetic	Motor
Li et al. (2014)	240,000	3.175	762,000	2.79	Aerostatic	Air turbine
Müller et al. (2016)	466,000	3 & 3.175	1,479,550	1.7	Aerostatic	Air turbine

by aerostatic bearings. Two spindle prototypes were developed, and their performances including the rotational speed, rotational accuracy and machining results were evaluated.

2 Compact Air Bearing Spindles for Micro Machining

Ultra high speed air bearing spindles, driven by air turbines, were developed at the Institute for Manufacturing Technology and Production Systems (FBK). These spindles reach a maximum rotational speed of 466,000 rpm. With small dimensions of $34 \times 24 \times 29$ mm and a weight of 165 g (type I) and $24 \times 36 \times 36$ mm and 220 g (type II), the spindles are well adapted to the requirements of desktop sized machine tools [6]. The shank of the micro tool (e.g. micro end mill, micro pencil grinding tool or electrical discharge machining (EDM) electrode) acts as the rotor and is thus a part of the spindles' bearing system; no further chucking is necessary. With this configuration, the tool run-out error only depends on the accuracy of manufacturing of the air bearing stator and the tool itself. The axial bearing is designed as a ball to plate plain bearing (type I) preloaded by magnetic force or aerostatic thrust bearings (type II). Figure 1 shows a schematic sketch of the aerostatic spindles and the build prototypes.

Two types of bearings are used in the spindles. (a) inlet compensated [16] and (b) outlet groove-compensated [17] journal bearings. Axially inlet compensated thrust

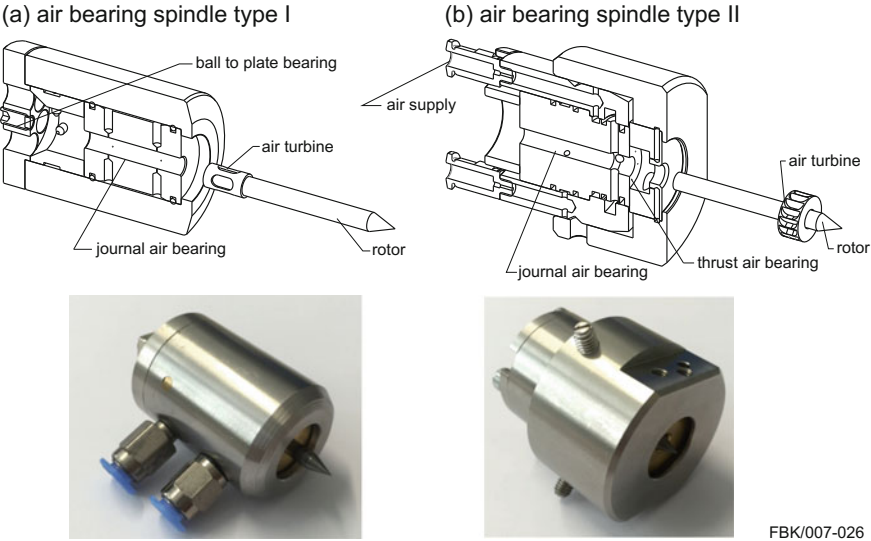


Fig. 1 Schematic of the aerostatic spindles and build prototypes

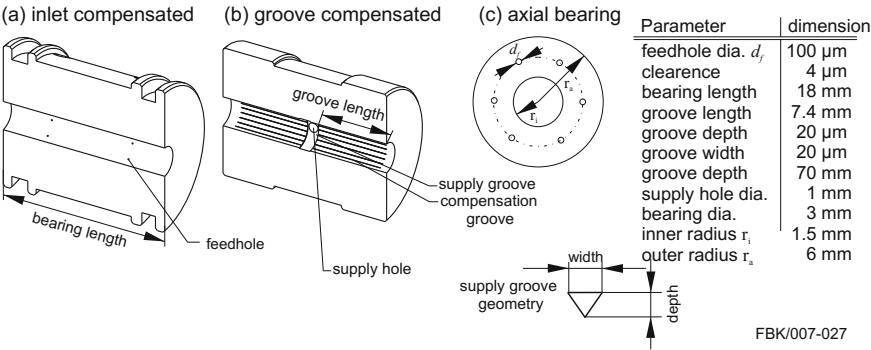


Fig. 2 Aerostatic bearing design **a** inlet compensated journal bearing, **b** groove compensated journal bearing, **c** thrust bearing (feedholetype inherent)

bearings (c) are applied. Figure 2 shows a schematic sketch of the bearings and their relevant geometrical properties.

2.1 Numerical Simulation of the Air Bearings

The behavior of the aerostatic bearings, which are used in the spindles, is determined by the inlet flow effects near the micro drilled feedholes (Fig. 2) [18]. A deep

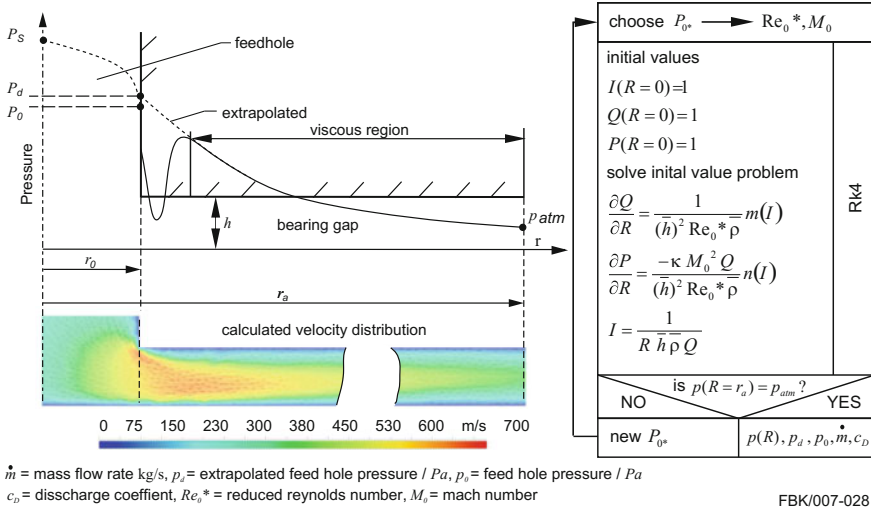


Fig. 3 Entrance region of air bearing, notation (left) and solution procedure (right)

understanding of these flow phenomena and accurate prediction of their relevant parameters (e.g. mass flow rate or discharge coefficient) are essential for the design and optimisation of aerostatic bearings [19]. One method to obtain the flow phenomena at the feeding sources is to transform the Reynolds equation equations in the bearing gap to an initial value problem, which is a system of Ordinary Differential Equations (ODE) with values (P dimensionless pressure p/p_a , I velocity integral function, Q velocity amplitude function) [20].

This ODE system is solved numerically via the 4th order Runge Kutta method (RK4) with adaptive step size in a first step [21]. One result of this numerical simulation is the pressure profile from the feedhole to the end of the stator (narrow channel solution). In a second step, the theoretical pressure p_d at the feeding sources can be obtained by extrapolating the pressure curve of the viscous film region to the feeding hole (Fig. 3). In the steady state case p_d is a function of the feedhole and bearing geometry, the supply pressure p_s and the air gap between the bearing surfaces (rotor/stator). Figure 3 shows a schematic section of an air bearing (left) and the solution procedure on the right side. The solving of the initial value problem started by choosing the feedhole pressure $P_0^* = p_0^*/p_{atm}$. With this value, the reduced Reynolds number Re_0^* and the mach number M_0 at the feedhole can be calculated. Then, the initial value system is solved from the feedhole radius r_0 to the end of the bearing r_a . The next step is checking if the pressure at $p(R=r_a)$ is equal to the atmospheric pressure $p_{atm} = 101,000$ Pa. If this is the case, the relevant feeding parameters can be calculated. If $p(R=r_a) \neq p_{atm}$, P_0^* needs to be adapted. For this, an adaptive method is implemented into the solution procedure. $n(I)$ and $m(I)$ are characteristic help functions and $\bar{\rho}$ is the dimensionless density in relation to the density

of air under standard conditions. A detailed derivation of the mathematics of this method is described by Tang [22].

Calculation of pressure distribution and bearing characteristics. The fluid film in the bearings is calculated by the dimensionless compressible Reynolds equation (1) [23]:

$$\operatorname{div} (PH^3 \operatorname{grad} (P) - \Lambda PH) = \sigma \frac{\partial}{\partial \tau} (PH) \quad (1)$$

Thereby P is the dimensionless pressure p/p_{atm} with p_{atm} is the atmospheric pressure 1 bar, H the dimensionless clearance h/c between the bearing surfaces regarding to the coaxial clearance c , Λ is the bearing number, σ the squeeze number and τ the normalised time:

$$\Lambda = \frac{6\mu\omega r^2}{p_{atm}h^2} \quad \sigma = \frac{12\mu\nu}{p_{atm}} \left(\frac{r_a}{h} \right)^2 \quad \tau = \nu t \quad (2)$$

Numerical method: Integration of Eq. (1) over a control surface and applying the Gauss's divergence theorem results in [23]:

$$\oint_{\Gamma_{ij}} (PH^3 \nabla P - \Lambda PH) \hat{n} \cdot d\mathbf{l} = \sigma \frac{\partial}{\partial \tau} \int \int_{\Sigma_{ij}} (PH) dx dy \quad (3)$$

The left side of this equation represents a boundary integral, which must be calculated over the contour of the control surface Γ , the right side of the equation is a surface integral of the time-dependent term. The equation is solved numerically with the Finite Volume Method (FVM). Figure 4 shows exemplarily a physical mesh of a thrust bearing (a). This mesh is transformed into a reference mesh (c) ξ, η -system. The mesh flux through the boundary integral is calculated with a 9-point element (b) on 8 sides of the 2D control surface. The boundary conditions of the bearings are atmospheric pressure $p_{atm} = 101,000$ Pa for the inner and the outer boundary of the bearing and the theoretical inlet pressure p_d at the feeding sources (Fig. 3). For the steady state case, the equation system for the 2D control surfaces is solved via Newton Raphson method [21].

Static results. The static pressure distribution of the air bearings can be calculated with Eq. (3) by ignoring the right hand side (time-dependent term of Eq. 1). Figure 5 shows the dimensionless pressure distribution of the three types of aerostatic bearings. The following static bearing characteristics can be calculated with this pressure distribution.

Friction loss P : In the developed micro machining spindles, the friction loss of the air bearings is much higher than the cutting power of a micro tool (ca. 0.8 W for an 50 μ m diameter micro end mill) and thus more important for the design of the drive system [8]. The friction loss in aerostatic journal P_j and thrust bearings P_t can be calculated using Petroff's equation. The viscous friction loss of the bearings depends on the bearing geometry, viscosity of the air, rotational speed and thickness

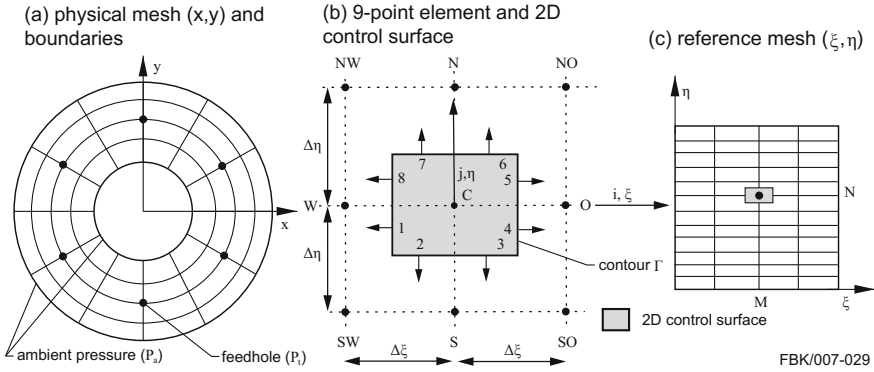


Fig. 4 Mesh with boundary conditions and 2D control surface with the 8 fluxes, mesh size $M \times N$. **a** Physical mesh for a thrust bearing, **b** 9-point element and 2D control surface, **c** reference mesh

Table 2 Overview of the calculated static bearing characteristics at $e = 0.4 \mu\text{m}$ (Fiction loss at 300.000 rpm)

Bearing type		Friction loss [P]/W	Load capacity [P]/W	Static stiffness [K _s]/N/μm	Mass flow rate [ṁ]/kg/s
Thrust		4.65	5.46	2.88	9.96×10^{-6}
Journal	Inlet-compensated	2.02	1.25	1.82	11.93×10^{-6}
	Groove comp.	1.82	0.61	1:63	10.21×10^{-6}

of the air film. The friction power loss of a journal P_j and thrust P_t bearing is defined by [16], with the rotational frequency ω the bearing length L and diameter D :

$$P_j = \frac{\pi \mu \omega^2 L D^3}{4c} \quad P_t = \frac{\pi \mu \omega^2 (r_a^4 - r_i^4)}{2c} \quad (4)$$

r_a and r_i are the outer and inner radius of the thrust bearing (Fig. 2).

Load capacity W and static stiffness K_s : The load capacity of the bearings can be calculated by integrating the pressure profile over the bearing surface A . The static stiffness of an air bearing is defined as force per unit displacement, which can be calculated by using the difference method with deflection Δh . The load capacity and static stiffness of the air bearing is then defined as:

$$W = \int_A p dA \quad K_s = \frac{W(h_0 + \Delta h) - W(h_0)}{\Delta h} \quad (5)$$

Table 2 shows an overview of the calculated static results of the three types of bearings. The static stiffness and load capacity of the inlet-compensated bearing is higher compared to the groove compensated bearing.

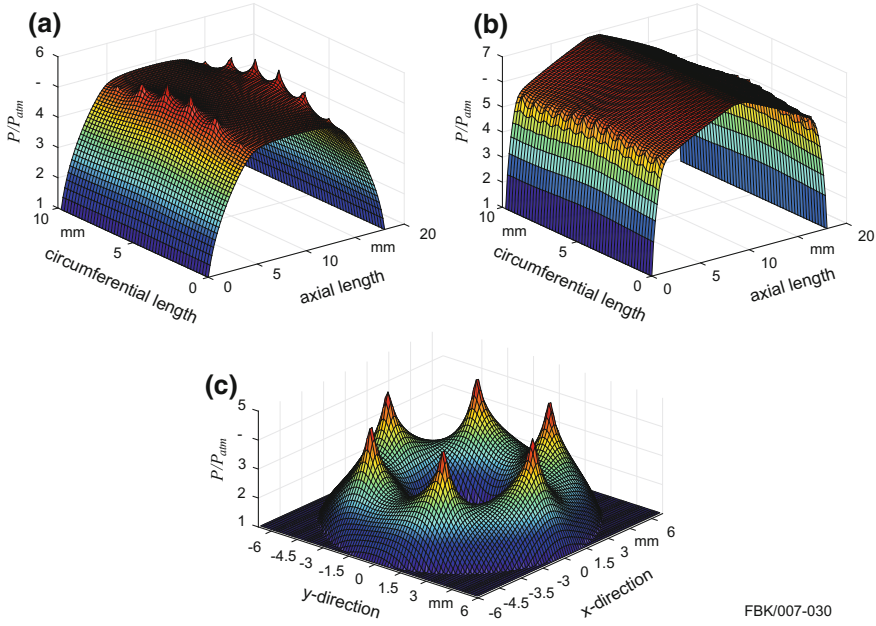


Fig. 5 Dimensionless pressure distribution of aerostatic journal bearings: **a** inlet-compensated journal bearing with 12 feed holes, **b** groove-compensated journal bearing with 12 supply grooves (both at $e = 0.4 \mu\text{m}$ eccentricity, $c = 4 \mu\text{m}$, $p_s = 8 \text{ bar}$) and thrust bearing with 6 feed holes

Dynamic results. The dynamic stiffness and damping characteristic of the air bearings are calculated with the linear perturbation method. Thereby, a small perturbation of the gap height ($H = H_0 + \Delta = H_0 + \Delta H e^{i\omega\tau}$) is applied to Eq. (3). Cancelling all static terms and terms higher than first order this results in:

$$\oint_{\Gamma_{ij}} [(3P_0 H_0^2 \Delta H + H_0^3 \Delta P) P_0 + P_0 H_0^3 \Delta P - \Lambda (P_0 \Delta H + H_0 \Delta P)] \hat{n} \cdot d\mathbf{l} = i\sigma \int \int_{\Sigma_{ij}} (P_0 \Delta H + H_0 \Delta P) dx dy \quad (6)$$

Equation 6 is a system of linear equations of the form $A(H_0, P_0, \omega) \cdot x = b$. H_0 is the static clearance between the bearing surfaces and ΔH the small perturbation of the clearance with the perturbation frequency ω . The corresponding pressure in the bearing will then have the form: $P = P_0 + \Delta P e^{i\omega\tau}$ with P_0 as the static pressure (Fig. 5) and ΔP as the fluid film reaction to the applied perturbation. Then, the dynamic stiffness k and damping characteristic c for the bearing can be obtained by integrating the real (stiffness) and imaginary (damping) part of ΔP over the bearing surface (Eq. 7). A detailed description of this method is presented by Hakwoon et al. [24].

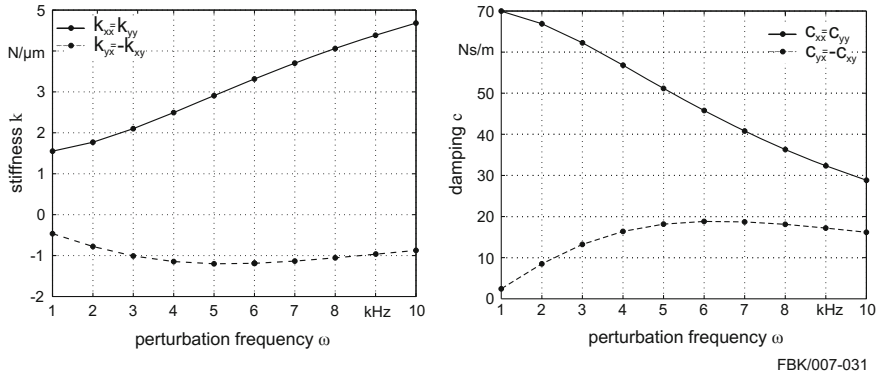


Fig. 6 Dynamic direct K_{ii} and cross-coupled C_{ij} stiffness and damping properties of the groove compensated journal bearing

$$-\Delta P = \Delta P_K + i\omega \Delta P_c \quad k = -p_a \int_A \Delta P_k \quad c = -p_a \int_A \Delta P_c \quad (7)$$

Figure 6 shows exemplarily the calculated stiffness and damping coefficients for a journal bearing (groove compensated). The coefficients respectively represent the direct stiffness and damping behavior (K_{ii} and C_{ii}) of the supporting fluid film, while the two other coefficients describe the cross-coupled behavior K_{ij} and C_{ij} .

Generally, the dynamic stiffness of an air bearing reaches an asymptotic value at high perturbation frequencies (rotational speeds), while the damping of the bearings tends to zero Fig. 6 [25]. For groove-compensated journal bearings, simulation-based parameter studies reveal that the coefficients of these bearings are negatively influenced by an increasing dead volume that results from the broached compensation grooves. For inlet-compensated journal bearings the coefficients are strongly influenced by the feedhole geometry.

2.2 Stability Analysis

A rotordynamic model was built in ANSYS 17.0^{®1} based on the calculated stiffness and damping coefficients. With this model, critical speeds are calculated (eigenfrequencies and half frequency whirl). In the model, predefined virtual bearing elements (COMB1214) are used for the journal bearings. These elements allow to define stiffness and damping characteristics in two perpendicular directions (K_{ii} , C_{jj}) as well as cross-coupled terms (K_{ij} , C_{ij}) [26]. For the thrust bearings, predefined virtual spring

¹Naming of specific manufacturers is done solely for the sake of completeness and does not necessarily imply an endorsement of the named companies nor that the products are necessarily the best for the purpose.

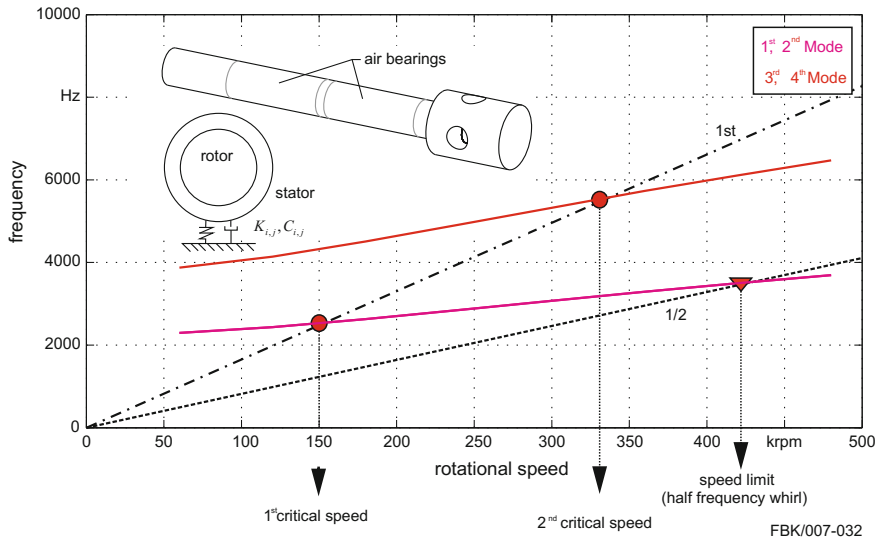


Fig. 7 Campbell diagram result chart of rotordynamic analysis for spindle type I

damper elements (COMBIN14) are applied. Figure 7 shows the results of the rotordynamic analysis in a Campbell diagram, in which the evolution of the natural frequencies with rotational velocities for spindle type I can be found (groove compensated bearing). A rotational velocity range from 0 to 500,000 rpm with 10,000 rpm intervals is selected to create an adequate response curve. In this study, the first six natural frequencies and the vibration mode shapes are extracted. The first critical mode is at 150,000 rpm, the second at 330,000 rpm. The half frequency instability [27] of the rotor bearing system, which limits the maximum rotational speed of the spindle, starts at 433,000 rpm. For the spindle type II (not displayed) it starts at 400,000 rpm, due to the higher mass of the rotor and thus lower eigenfrequencies (Fig. 1).

2.3 Basic Performance Evaluations

The rotational speed of the developed spindles and the rotational accuracy was measured with two orthogonal capacitive probes (CPL190) (see Footnote 1) in x, y-direction. They were directed at a cylindrical tool shaft/rotor with a peak to peak run-out of $0.4\text{ }\mu\text{m}$ and a cylindricity of $1\text{ }\mu\text{m}$. The maximum sampling rate of the sensor is 15 kHz, thus rotational frequencies up to 7.5 kHz can be estimated. In addition, a microphone was used to measure the spindles' sound frequencies above 7.5 kHz. Figure 8 shows a waterfall Fast Fourier Transformation (FFT) plot of a run up experiment of spindle type I. The dominating peak in the FFT is equal to the ro-

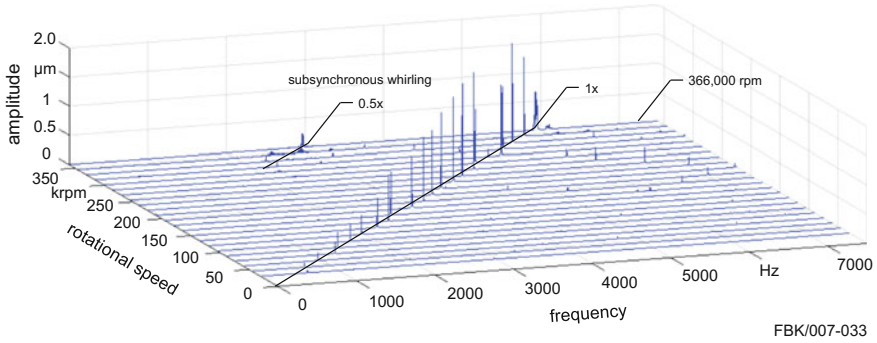


Fig. 8 Waterfall FFT plot of the measured rotor frequency during run-up from 0 to 366,000 rpm (spindle type I)

tational frequency caused by excitation due to unbalance. Subsynchronous whirling of the tested spindle can be observed at rotational speeds above 350,000 rpm. Below 350,000 rpm, the spindle does not show disturbing frequencies. Consequently, the maximum achievable rotational speed of the spindle with the applied cylindrical tool shaft is 366,000 rpm. When a micro tool is inserted in the spindle instead of the cylindrical shaft, the spindle reaches 466,000 rpm (measured by the microphone) because of an approx. 20% lower mass of the micro tool compared to the tool shaft/rotor test sample, resulting in higher eigenfrequencies of the system.

3 Micro Machining Experiments

Micro milling tests were performed with spindle type I. The spindle was installed into a 3-axis machine tool (for specifications of the machine tool [28]). Test chan-

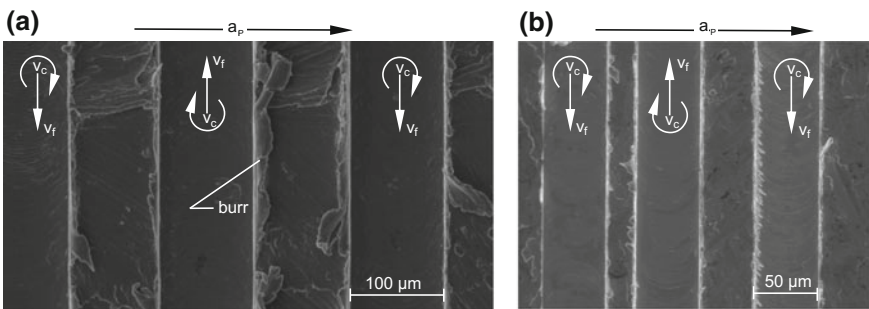


Fig. 9 Micro machining with 100 μm and 50 μm micro end mills of **a** cp-titanium and **b** brass with increasing depth of cut $a_p = 5, 7, 10 \mu\text{m}$, $v_f = 300 \text{ mm/min}$ at $n = 300 \text{ krpm}$

nels were milled with different depths of cut a_p (5–10 μm) in CP titanium grade 2 and brass (CuZn40Pb). To both materials a feed rate of 300 mm/min at 300,000 rpm was applied. For titanium, a micro end mill with a diameter of 100 μm was used and for brass a micro end mill with a diameter of 50 μm . Both end mills are single edged and optimised for a feed per tooth of 1–3 μm [28]. With the applied rotational speed of 300,000 rpm, typical cutting speeds of 94.25 m/min for titanium [29] and 47.12 m/min for brass resulted. Figure 9 depicts Scanning Electron Microscope (SEM) images of the machined channels. The bottom surface of the channels is homogeneous which suggests a low deviation of the rotational speed during machining. In addition, the size of the burrs is not increasing with the depth of the cut. Generally, the quality of the machined channels is very good. It is similar to the results which were machined on the same 3-axis machine with a commercially available main spindle (ABLM125) (see Footnote 1) [28]. Actually, due to the achievable high rotational speeds, higher material removal rates with the same quality can be reached by keeping the feed per tooth constant at rising feed rates.

4 Conclusion

In this paper, two small air bearing spindles (types I and II), developed for the implementation in desktop-sized machine tools, are introduced. Both spindles are driven by air turbines and the tool shank of the micro tool is directly used as the rotor. With this configuration, no further chucking for the micro tool is necessary.

The modeling techniques for the air bearings via FVM simulations have been presented. These techniques can be used to optimise the bearing characteristics. One result of the simulations is that the calculated stiffness and damping characteristics of the groove-compensated journal air bearings strongly depend on the dead volume generated by the compensation grooves. For the inlet-compensated air bearings, the prediction of the flow effects at the feeding sources and their relevant parameters (pressure at feedhole, mass flow rate) is important. The calculated stiffness and damping coefficients were used to build a rotordynamic model of the spindle. With this model, critical speeds (eigenfrequencies and half frequency whirl) are calculated. A basic performance evaluation for both spindles was conducted. For this purpose two orthogonal capacitive probes were used to measure the rotational accuracy and speed. Up to 7.5 kHz a microphone was used to measure the spindles' sound frequencies. The spindle type I reaches a very high maximal rotational speed of 466,000 rpm.

This spindle was implemented in a desktop-sized machine tool and was used for micro milling of titanium and brass at 300,000 rpm. SEM images of the machined channels show that the bottom surface was very homogeneous which suggests a low deviation of the rotational speed when micro machining and the size of the burrs was not increasing with the depth of the cuts. In general the quality of the machined channels was similar to the results, which were machined on the 3-axis machine with the equipped main spindle. With the high rotational speed of the developed spindles, higher material removal rates can be achieved by keeping the feed per tooth

constant at rising feed rates. Thus, the productivity of the micro machining process is enhanced.

References

1. Dornfeld, D., Mina, S., Takeuchi, Y.: Recent advances in mechanical micromachining. *CIRP Ann. Manuf. Technol.* **55**(2), 745–768 (2006)
2. Aurich, J.C., Reichenbach, I.G., Schüler, G.M.: Manufacture and application of ultra-small micro end mills. *CIRP Ann. Manuf. Technol.* **61**(1), 83–86 (2012)
3. Aurich, J.C., Engmann, J., Schüler, G.M., Haberland, R.: Micro grinding tool for manufacture of complex structures in brittle materials. *CIRP Ann. Manuf. Technol.* **58**(1), 311–314 (2009)
4. Grimske, S., Kong, N., Röhlig, B., Wulfsberg, J.P.: Square foot manufacturing—a modular and mutable desktop machine tool system. *Mech. Based Des. Struct. Mach.* **42**(3), 386–397 (2014)
5. Arrabiyeh, P.A., Kirsch, B., Aurich, J.C.: Development of micro pencil grinding tools via an electroless plating process. In: *Proceedings of the 11th International Conference on Manufacturing Science and Engineering* (2016)
6. Wulfsberg, J.P., Grimske, S., Kohrs, P., Kong, N.: Kleine Werkzeugmaschinen für kleine Werkstücke. *wt Werkstattstechnik online* **100**(11), 190–194 (2010)
7. Jackson, M.J., Robinson, G.M., Hyde, L.J., Kanjarkar, K., Chie, J.: Design and manufacture of high-speed spindles for dry micromachining applications. *Int. J. Nanomanuf.* **1**(5), 641–656 (2008)
8. Müller, C., Reichenbach, I.G., Aurich, J.C.: Design and numerical simulation of an air turbine for a high frequency tool spindle. In: *9th International Conference on Micro Manufacturing* (2014)
9. D.D., Jokiel Jr., B., Ziegert, J.C., Payne, S.W.T., Pathak, J.P.: Next generation spindles for micromilling. *Sandia Report* (2004)
10. Sung, H.: High-speed fluid bearing micro-spindles for meso-scale machine tools (mMTs). *Dissertation Northwestern University* (2007)
11. Delhaes, G.M.J., van Beek, A., van Ostayen, R.A.J., Munnig Schmidt, R.H.: The viscous driven aerostatic supported high-speed spindle. *Tribol. Int.* **42**(11/12), 1550–1557 (2009)
12. Jahanmir, S., Ren, Z., Heshmat, H., Tomaszewski, M.: Design and evaluation of an ultrahigh speed micro-machining spindle. *Int. J. Mach. Sci. Technol.* **11**(2), 224–243 (2010)
13. Jahanmir, S.: Surface integrity in ultrahigh speed micromachining. In: *Proceedings of the 1st CIRP Conference on Surface Integrity*, pp. 156–161 (2011)
14. Kimman, M.H.: Design of a micro milling setup with an active magnetic bearing spindle. *Dissertation Technical University Delft* (2010)
15. Li, W., Zhou, Z.X., Xiao, H., Zhang, B.: Design and evaluation of a high-speed and precision microspindle. *Int. J. Adv. Manuf. Technol.* **78**(5), 997–1004 (2015)
16. Powell, J.W.: *Design of Aerostatic Bearings*. Machinery Publishing, pp. 181–198 (1970)
17. Wardle, F.: *Ultra-Precision Bearings*, 1st Edn. Woodhead Publishing (2015)
18. Hassini, M.A., Arghir, M., Frocot, M.: Comparison between numerical and experimental dynamic coefficients of a hybrid aerostatic bearing. *J. Eng. Gas Turbines Power* **134**(12) (2012)
19. Arghir, M., Hassini, M.A., Balducci, F., Gauthier, R.: Synthesis of experimental and theoretical analysis of pneumatic hammer instability in an aerostatic bearing. *J. Eng. Gas Turbines Power* **138** (2016)
20. Waumans, T., Al-Bender, F., Reynaerts, D.: A semi-analytical method for the solution of entrance flow effects in inherently restricted aerostatic bearings. *Proc. ASME Turbo Expo* **5** (2008)
21. Rao, S.B., Shantha, C.K.: *Numerical Methods: With Programs in BASIC, FORTRAN, Pascal and C++*. Universities Press (2004)

22. Tang, I.C.: Inertia effects of air in an externally pressurized gas bearing. *Acta Mechanica* **5**(1), 71–82 (1968)
23. Gross, W.A.: *Fluid Film Lubrication*. Wiley-Interscience, New York (1980)
24. Hakwoon, K., Gunhee, J., Heonjeong, H.: A generalized Reynolds equation and its perturbation equations for fluid dynamic bearings with curved surfaces. *Tribol. Int.* **50**, 6–15 (2012)
25. Waumans, T., Vleugels, P., Peirs, J., Al-Bender, F., Reynaerts, D.: Rotordynamic behaviour of a micro-turbine rotor on air bearings: modelling techniques and experimental verification. *Proc. ISMA* (2006)
26. ANSYS Inc.: ANSYS help version **17**, 2016
27. Rao, J.S.: *History of Rotating Machinery Dynamics*. Springer (2011)
28. Bohley, M., Reichenbach, I.G., Müller, C., Aurich, J.C.: Development of a desktop machine tool for integrated ultra-small micro end mill production and application. In: *Proceedings of the 11th International Conference on Micro Manufacturing Paper* **13**, pp. 1–6 (2016)
29. Melkote, S.N., Liu, R., Fernandez-Zelaia, P., Marusich, T.: A physically based constitutive model for simulation of segmented chip formation in orthogonal cutting of commercially pure titanium. *CIRP Ann. Manuf. Technol.* **64**, 65–68 (2015)

Small Machine Tools for Small Workpieces
Final Report of the DFG Priority Program 1476
Wulfsberg, J.P.; Sanders, A. (Eds.)
2017, XIII, 229 p. 188 illus., 148 illus. in color.,
Hardcover
ISBN: 978-3-319-49267-4